


Research Article

East Asian monsoon variations in the loess–desert transitional zone (northern China) during the past 14 ka and their comparison with TraCE21K simulation results

Yao Gu¹, Huayu Lu¹ , Jingjing Wang¹, Hongyan Zhang¹, Wenchao Zhang², Chenghong Liang¹ and Jiang Wu^{1,3}

¹School of Geography and Ocean Science, Nanjing University, Nanjing 210023, China; ²School of Earth Sciences and Resources, China University of Geosciences (Beijing), Beijing 100083, China and ³School of Geography, Nanjing Normal University, Nanjing 210023, China

Abstract

The Holocene is a critical period for understanding the East Asian monsoon system (EAM) over long timescales, but high-precision dating and high-resolution records from the Holocene epoch at monsoonal margins of East Asia are lacking. Here, on the basis of closely spaced radiocarbon and optically stimulated luminescence dating results obtained from a typical loess–paleosol sequence on the northern Chinese Loess Plateau (CLP), we provide an independent age-based, high-resolution depositional record of East Asian summer (EASM) and winter monsoons (EAWM) variations over the past ~14 ka. We find that both the EASM and EAWM simultaneously strengthened sometime during the Holocene optimum (~7–5 ka BP), with greater seasonality, and weakened during the Late Holocene. These findings are counter-intuitive to our understanding of the EAM variations based on loess records at suborbital scales during interglacial periods, providing an alternative scenario of the monsoon system evolution. We postulate that high-latitude forcing and surface feedbacks, such as vegetation change, have modulated the EAM variations during the Holocene warmth.

Keywords: East Asian monsoon, Radiocarbon dating, Holocene, Loess, TraCE21K

(Received 6 February 2023; accepted 3 December 2023)

INTRODUCTION

The Holocene has experienced considerable climate variability (Bond et al., 2001; Cai et al., 2021), and these climatic changes have been reported from all latitudes (Routson et al., 2019; Walczak et al., 2020; Bova et al., 2021; Cai et al., 2021; Liang et al., 2022). It is also recognized that there is regional diversity in Holocene climate variations in East Asia influenced by the East Asian monsoon system (EAM) circulation. However, the phase relationship between the East Asian summer (EASM) and winter monsoons (EAWM) (e.g., Wen, X.Y. et al., 2016) and their seasonal evolution have not yet been determined. Loess deposits on the Chinese Loess Plateau (CLP) constitute an excellent proxy record of the EASM and EAWM variations at multiple timescales, and provide an opportunity to address these questions. The loess deposits were originally transported by the EAWM (Li et al., 1988; An, 2000; Lu et al., 2022), their grain size and dust sedimentation rate (DSR) are proxy indicators of the EAWM strength (Lu and Sun, 2000; Lu et al., 2022). Meanwhile, magnetic susceptibility, organic matter content, and carbon and hydrogen isotopic compositions of loess deposits are direct proxies of the EASM intensity, indicated by precipitation (Wang et al., 2021; Liang et al., 2022; Lu et al., 2022). Hence, the loess deposits

provide one of the best records for reconstructing the variability in the EASM and EAWM at high resolution concurrently, avoiding the problems that the EASM and EAWM variations cannot be compared under a similar timescale.

The loess–desert transitional zone in northern China has long been thought to be sensitive to climate change and human influences. Small changes in vegetation, climate, or land use in this region will drive major changes in surrounding sand dunes and transportation and deposition of aeolian dust (Wang et al., 2019; Xu et al., 2020). In this region, the widespread aeolian deposits have recorded the history of environmental change under the influence of the EAM circulation and global climate change (Lu et al., 2005, 2011). In this study, on the basis of a loess–paleosol record in the loess–desert transitional zone in northern China (Fig. 1), a high-resolution record of the EASM and EAWM variations since ~14 ka is obtained. The results reveal novel behaviours of the EAM seasonal variability during a warm period.

MATERIALS AND METHODS

Geographic setting

The Zhenbeitai (ZBT) section (38°19′41.9″N, 109°43′51.4″E; 1187 m above sea level) is located in the transitional zone between monsoon humid and Asian interior arid regions: the CLP and the Mu Us sand fields. The mean annual temperature at this site is ~8.0°C, and the mean annual precipitation is ~400 mm. Most

Corresponding author: Huayu Lu; Email: huayulu@nju.edu.cn

Cite this article: Gu Y, Lu H, Wang J, Zhang H, Zhang W, Liang C, Wu J (2024). East Asian monsoon variations in the loess–desert transitional zone (northern China) during the past 14 ka and their comparison with TraCE21K simulation results. *Quaternary Research* 120, 53–61. <https://doi.org/10.1017/qua.2023.76>

© The Author(s), 2024. Published by Cambridge University Press on behalf of Quaternary Research Center



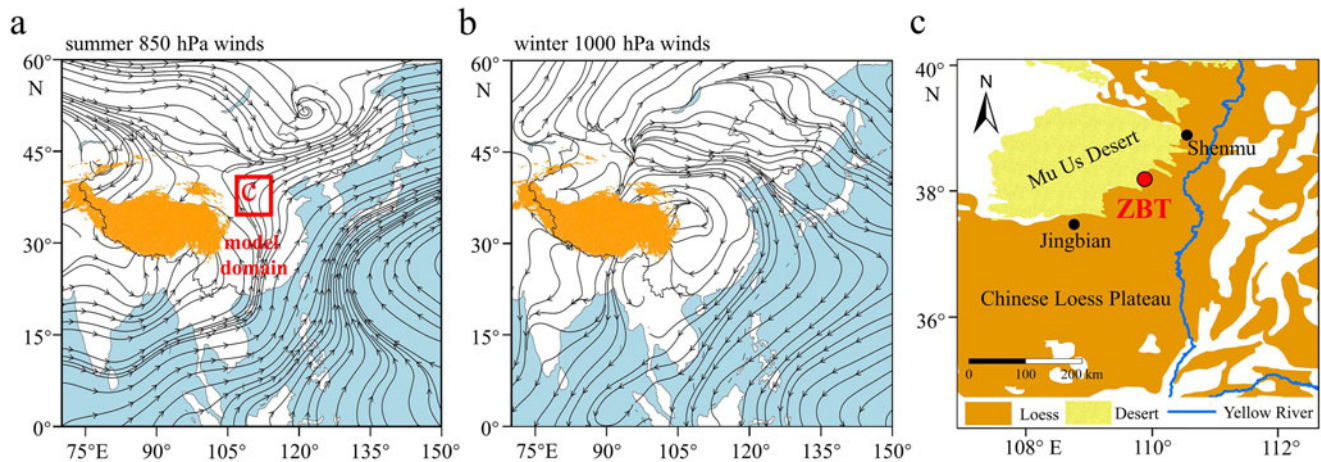


Figure 1. Climatological mean wind conditions in boreal summer (June–July–August) and winter (December–January–February) and sampling site at Zhenbeitai (ZBT). (a) Summer mean 850 hPa streamline based on NCEP reanalysis data from 1980 to 2010 (Kanamitsu et al., 2002). The red rectangle is the area shown in c (107–114°E, 33–41°N). (b) Winter mean 1000 hPa streamline based on NCEP reanalysis data from 1980 to 2010 (Kanamitsu et al., 2002). (c) Sampling site at ZBT and some other records in the loess–desert transitional zone.

precipitation falls in the summer season, in a typical monsoon climate (Wang et al., 2019; Liang et al., 2022).

The exposed studied section has a thickness of 16.8 m. The upper 0–0.6 m is a light yellow-brown sandy loam soil with some modern plant roots. A dark yellow-brown paleosol layer from 0.6 to 2.9 m underlies the upper unit. Below this is a dark brown, sandy soil layer from 2.9 to 3.3 m and a sand layer from 3.3 to 5.1 m that overlies a thick loess layer that extends to the bottom of the section.

After 30–50 cm of surface sediments were excavated to avoid contamination, a total of 44 loess samples were collected from the upper 5.1 m of the section at intervals of 10 cm above 3.3 m and 20 cm below 3.3 m for accelerator mass spectrometry (AMS) radiocarbon dating.

Radiocarbon dating

The humin fraction of the loess samples was extracted following the acid–alkaline–acid method for AMS radiocarbon dating (Hajdas, 2008). All samples were dried thoroughly at room temperature; visible plant remains were removed with tweezers. HCl (2 N) was used for at least 4 hours at room temperature to completely remove carbonates. After samples were rinsed with ultrapure Milli-Q deionized water to a pH of ~6, a series of 0.5% NaOH washes was added to remove the base-soluble fraction (i.e., humic acids) based on the concentration of humic acids. NaOH washes were conducted until the solution became clear, and the remainder was rinsed with deionized water three times. Then, 1 N HCl was added, and after acid washing, the samples were rinsed with deionized water to neutral pH and dried at 60°C.

All samples were combusted in an online combustion system in a mixture of O₂ and He gas atmosphere at 920°C. Then, water was eliminated, and the extracted CO₂ was converted to graphite in the reaction CO₂ + H₂ → C + H₂O with ~5 mg of iron catalyst at a temperature of 550°C. All ¹⁴C measurements were undertaken on graphitized samples at the Laboratory of AMS Dating and the Environment at Nanjing University using a compact radiocarbon AMS dating system (MICADAS; Synal et al. 2007). Conventional radiocarbon ages were converted to

calendar ages using OxCal online v. 4.4 (Ramsey, 2009) and the IntCal20 calibration curve (Reimer et al., 2020), except for the 0.1 m sample, for which the post-bomb atmospheric NH zone 2 curve was used (Hua et al., 2013).

Age–depth modelling

Bayesian age–depth modelling was performed using the Bacon code (Blaauw and Christen, 2011) based on 44 radiocarbon ages and 20 OSL ages for the ZBT site (Wu et al., 2019). We first performed modelling with the default prior information: sedimentation (sed.) shape = 1.5 and acc. mean = 20 for the gamma distribution; and memory (mem.) mean = 0.7 and mem. strength = 4 for the beta distribution, describing the memory effects of the DSR. Then, based on the first modelling results, we adjusted the parameters and reran the model to obtain our age–depth results. The final prior information used in this case was as follows: acc. shape = 1.5 and acc. mean = 20 for the gamma distribution; and mem. mean = 0.4 and mem. strength = 25 for the beta distribution. The IntCal20 calibration curve was used to convert the conventional radiocarbon ages input to calendar ages, and age modelling was run to achieve a 1 cm final resolution (Fig. 2). The ages were expressed in years before present (BP), where “present” is defined as 1950 CE.

DSR

DSR was calculated using the age–depth model as follows:

$$\text{DSR} = (d_2 - d_1)/(a_2 - a_1)$$

where d_1 and d_2 are consecutive depths and a_1 and a_2 are weighted mean model ages in the profile.

Numerical simulations

TraCE21K is a transient simulation of global climate evolution in the last 21,000 yr in the fully coupled Community Climate System v. 3 (CCSM3) (Liu et al., 2009; He and Clark, 2022). This simulation outputs a set of 4D model data sets to allow investigations

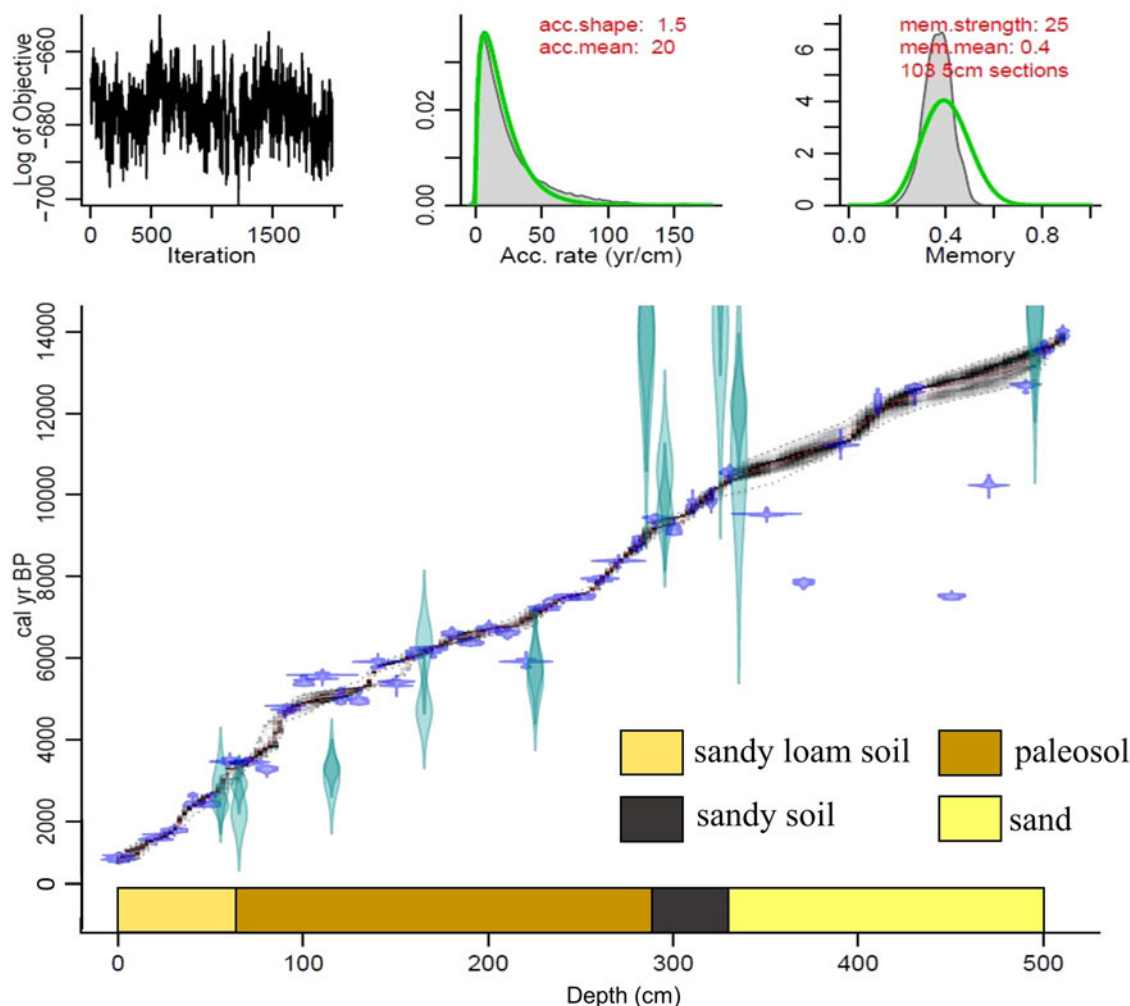


Figure 2. Age–depth model for Zhenbeitai (ZBT) loess–paleosol sequence based on 44 radiocarbon ages (this study) and 20 optically stimulated luminescence (OSL) ages (Wu et al., 2019). Blue denotes the ^{14}C ages, and green denotes OSL ages.

of coupled atmosphere–ocean–sea ice–land surface mechanisms and terrestrial ecosystem feedbacks. We selected boreal summer (June–July–August) precipitation as an index of the EASM and boreal winter (December–January–February) wind at 1000 hPa level as an index of the EAWM over the CLP (107–114°E, 33–41°N, as shown in the range of Fig. 1c) to obtain simulation records of EAM variations over the past 14 ka in TraCE21K (Wen X.Y. et al., 2016; Wang et al., 2023).

The outputs of TraCE21K show that all forcings (ALL), insolation forcing (Orbit), greenhouse gases (CO_2), meltwater flux forcing (MWF), and ice-sheet forcing (Ice Sheet) separately modulated EASM and EAWM variations during the Holocene optimum (Liu et al., 2009; Otto-Bliesner et al., 2014; Wen X.Y. et al., 2016; Wang et al., 2023; Supplementary Figs. S1–S3).

RESULTS AND DISCUSSION

Enhanced EAM seasonality during the Holocene optimum

Forty-four samples were obtained from ZBT for AMS radiocarbon dating (Fig. 2, Supplementary Table S1). An additional 20 optically stimulated luminescence (OSL) dating ages from the ZBT section were collected previously (Wu et al., 2019).

Combining these two sets of data, we built an independent time-scale for ZBT loess–paleosol deposits over the past 14 ka (Fig. 2). Along with this timescale, magnetic susceptibility at ZBT section, total organic carbon, and leaf wax n -alkane δD values of C29 at ZBT section are used as proxies for EASM strength (Liang et al., 2022), while the DSR distribution is a proxy of EAWM strength (Lu and Sun, 2000; Lu et al., 2022).

The DSR shows remarkable variations during the Holocene (ranging from 9 to 147 cm/ka with an average of 39.91 cm/ka) (Fig. 3e and f), presenting the first evidence that the EAWM strengthened during the Holocene optimum, a warm and humid period in East Asia (Lu et al., 2005, 2013a; Chen et al., 2015). In contrast, grain-size variations do not necessarily coincide with DSR variations (Fig. 3d), which is similar to what was observed in a European high-resolution ^{14}C -dated loess record (Ujvari et al., 2017). These disagreements between grain size and DSR are likely due to grain size being impacted by complex processes at short timescales (Ujvari et al., 2016).

Grain size is a result of combined effects of local/regional atmospheric circulation and environmental settings, including factors such as topography (Mason et al., 1999), source distance (Ding et al., 2005; Yang and Ding, 2008; Yang et al., 2015), aridity of source and sink, and vegetation cover (Pye, 1995). Taking the

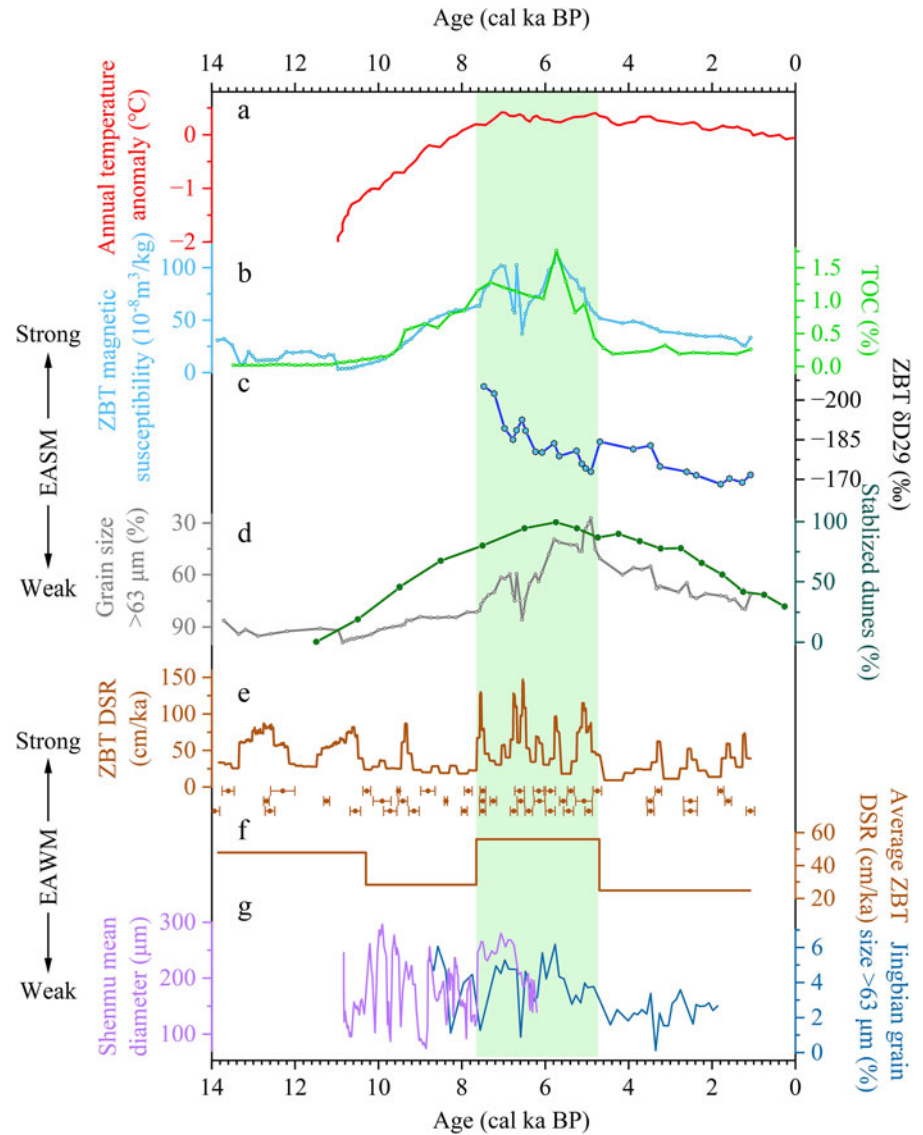


Figure 3. Synchronous strengthening of East Asian summer (EASM) and winter monsoons (EAWM) during the Holocene optimum. (a) Annual temperature anomaly trends from pollen-based reconstructions over the Northern Hemisphere landmass. The temperature anomaly is calculated against the recent 1 ka average annual temperature (Zhang et al., 2022). (b) Total organic carbon content (green line) (Lu et al., 2013a) and magnetic susceptibility (blue line) in the Zhenbeitai (ZBT) section. (c) Leaf wax *n*-alkane δD values of C29 in the ZBT section. Positive trend of δD values since the Mid-Holocene indicates both weakening of EASM and decrease in regional precipitation (Liang et al., 2022). (d) Grain size $> 63 \mu\text{m}$ in the ZBT section in this study (grey line) and percentage of stabilized dune sites in northern China (bottle-green line) (Xu et al., 2020). (e) Dust sedimentation rate (DSR) of ZBT. Dots under line e are 44 calibrated ^{14}C ages for ZBT, with an uncertainty interval of 2σ for ^{14}C ages. (f) Average DSR of ZBT. The average DSR was calculated for low-DSR Late Holocene period, high-DSR Mid-Holocene period, low-DSR Early Holocene period, and sand layer unit. (g) Other EAWM records in the loess–desert transitional zone (Wen X.H. et al., 2016; Gong et al., 2021). The locations of the records are shown in Fig. 1c. The green bar represents the period in which the EASM and EAWM synchronously strengthened.

example of ZBT, which is close to the Mu Us Desert dune fields, grain size is highly affected by the expansion and retreat of the dune fields, and large expansion and retreat in the Mu Us dune field has occurred since the last glacial maximum (Lu et al., 2005, 2013b). It is well known that the EASM was strong in the warm and humid climate of the Mid-Holocene (Lu et al., 2005, 2013a; Chen et al., 2015), as is further evidenced by the new proxies presented in this study (Fig. 3b–d). Stabilization of sand dunes in proximal dune fields is associated with strengthened EASM circulation; therefore, the maximum stabilization of dune fields occurred in the Mid-Holocene (Lu et al., 2005, 2013b; Xu et al., 2020; Fig. 3d, bottle-green line). An increased distance from the dust source would have led to an apparent decrease in grain size at the ZBT site. Thus, the grain-size variations were closely associated with sand dune changes, which are controlled by EASM precipitation. A fine particle size indicates a wetter climate in the transition zone between the loess and desert regions.

The DSR reflects only the number of particles deposited per unit time and area, which is determined by atmospheric loading, local trapping, and preservation conditions (Ujvari et al., 2017). The ZBT section is currently located at the margin of Mu Us dune fields. Surface sediments of the Mu Us dune field have

dominated coarse silt and fine sand deposition, and the sediment accumulation rate is closely associated with dune field surface processes. Meanwhile, EAWM circulation, which determines the Mu Us dune field surface processes and atmospheric loading in winter, has varied significantly during the Holocene, forced by boreal winter insolation (Wen X.Y. et al., 2016). At glacial–interglacial timescales, variations in vegetation can affect dust trapping and preservation, thus accounting for some portion of the DSR variations in the dune field marginal areas (Lu et al., 2013b). However, vegetation has not changed significantly during the Holocene on the CLP, as grasslands or grasslands with sparse trees have dominated this region throughout, leading to a nonsignificant change in vegetation (Jiang et al., 2013). Therefore, DSR is a direct and sensitive proxy index of EAWM strength, and a high DSR during the Holocene optimum corresponds to strengthened EAWM circulation. Some other records in the loess–desert transitional zone also indicate increased aeolian dust activities during the Holocene optimum (Wen X.H. et al., 2016; Gong et al., 2021; Fig. 3g), revealing a strengthened EAWM in this region.

Proxies of EASM intensity, such as magnetic susceptibility, total organic carbon, and leaf wax *n*-alkane δD values from the

ZBT section (Liang et al., 2022; Fig. 3b and c), indicate increased EASM precipitation in the Holocene optimum, thus providing direct evidence of the simultaneous strengthening of the EASM and EAWM (Fig. 3). This finding is counterintuitive to our understanding of EASM and EAWM variations in a warm period, as previously understood from Chinese loess records, in which a stronger EASM is associated with a weakened EAWM, and vice versa. However, our findings provide the first proxy-based evidence that the EASM and EAWM are concurrently strengthened.

Variations in EASM and EAWM in the past 14 ka are generally driven by solar radiation, high-latitude ice sheets, atmospheric CO₂, surface feedbacks such as vegetation changes, the El Niño–Southern Oscillation (ENSO), and the Atlantic Meridional Overturning Circulation (AMOC) (He et al., 2021). A strengthened EASM during some part of the Holocene optimum has been demonstrated by several types of proxies, such as lacustrine records (Chen et al., 2015), stalagmites (Wang et al., 2005; Cai et al., 2021), loess sediments (Lu et al., 2013a), and dune field change records (Lu et al., 2013b; Xu et al., 2020). Numerical simulation results have indicated that a strengthened atmospheric pressure gradient between the East Asian continent and adjacent ocean resulted in strengthened southerly winds (Wen X.Y. et al., 2016) and increased

precipitation (Sun et al., 2020), indicating a strong EASM during the Holocene optimum.

Although EASM variations generally track the insolation curve, there exists an ~3 ka delayed response to the summer insolation peak (Lu et al., 2005; Fig. 4a). This delay of the EASM peak relative to insolation forcing is thought to result from the impact of relict ice sheets (Lu et al., 2005) and atmospheric CO₂ forcing (Lu et al., 2013a). From the Early to Mid-Holocene, reduction of the residual Laurentide Ice Sheet (Lu et al., 2005, 2013a) could have enhanced EASM precipitation over northern China via atmospheric teleconnection. This enhancement cancelled out the insolation-induced precipitation decline and led to an enhanced EASM in the Mid-Holocene.

Similar to the EASM, the EAWM was also strengthened during some part of the Holocene optimum (Figs. 3 and 4), and this synchronous strengthening in the EASM and EAWM suggests that these two were separately forced. Sedimentary diatom assemblages and biogeochemical records from lacustrine sediments in southern China (Wang et al., 2012; Jia et al., 2015) and a record of vertical thermal structure changes from the southern China Sea (Steinke et al., 2011), as well as some grain-size proxies in the loess–desert transition zone (Wen X.H. et al., 2016; Gong et al., 2021; Fig. 3g), indicate an intensified EAWM sometime during

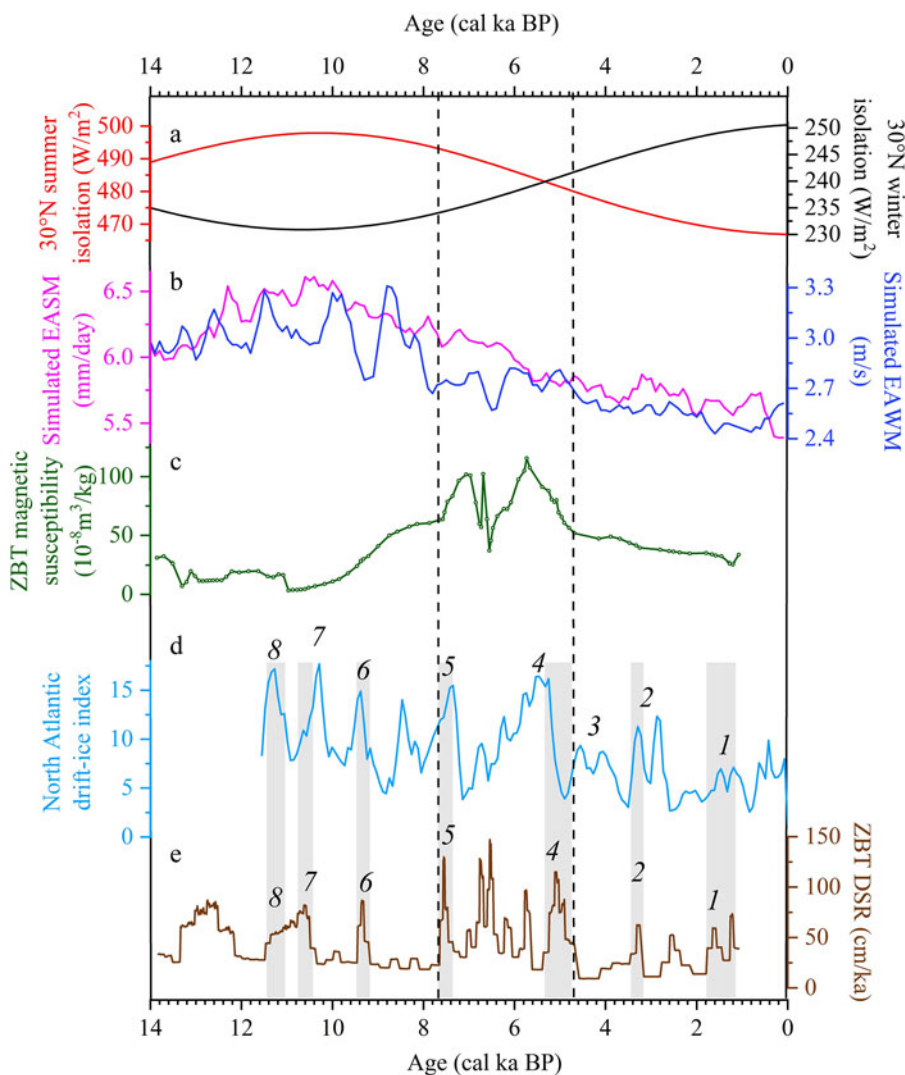


Figure 4. East Asian summer (EASM) and winter monsoon (EAWM) variations at millennial scales and the possible forcing mechanisms. (a) The 30°N summer (June–July–August) and winter (December–January–February) insolation (Laskar et al., 2004). (b) Numerically simulated EASM evolution as indicated by the average summer (June–July–August) precipitation over the Chinese Loess Plateau (CLP) (pink line) in TraCE21K and simulated EAWM evolution as indicated by the average winter (December–January–February) wind speed over the CLP (blue line). (c) Magnetic susceptibility of the Zhenbeitai (ZBT) section. (d) North Atlantic drift-ice records (Bond et al., 2001). (e) Dust sedimentation rate (DSR) of the ZBT section. Numbers above **d** and **e** represent Bond events 1–8, and the grey bars indicate high-DSR events correlated with North Atlantic cold events. The dashed lines indicate the Holocene optimum–strengthened EASM and EAWM.

the Holocene optimum. However, the EAWM as reconstructed based on grain size of loess in the central and south CLP is weak during the Mid-Holocene (Kang et al., 2020), which is different from our DSR record. This mismatch is likely due to grain size being a much more complex parameter that is affected by multiple factors; stochastic processes often have modulated grain-size distribution in specific regions (Ujvari et al., 2016). In our DSR record, the EAWM in the Early Holocene was not as intense as it was during the Holocene optimum, representing a delayed response of several thousand years relative to the winter insolation minimum (Fig. 4a). Perihelion shifts from boreal summer to winter from the Early to Late Holocene, as insolation was still relatively low in the Northern Hemisphere in winter during the Holocene optimum (~2–4% higher insolation than in the Early Holocene but ~4–7% lower compared with the present; Fig. 4a), may have resulted in low temperatures across the East Asian continent and thus enhanced land–sea temperature differences and winter monsoon circulation. However, this winter insolation forcing cannot explain the enhanced EAWM strength in the Holocene optimum compared with that in the Early Holocene, and other factors, such as high-latitude forcing and regional surface feedbacks, may be responsible for the strengthened EAWM circulation.

Our findings are in contrast to the hypothesis that the EASM and EAWM exhibit antiphase variations during this warm period. We interpret this discovery as having two implications: (1) Both the EASM and EAWM synchronously strengthened during some period of the Holocene optimum, suggesting that climate seasonality is enhanced during warming periods, with the dry season becoming drier and the wet season becoming wetter in a warming world. (2) The long-term EAM climate variations cannot be solely dominated by seasonal insolation changes, and high-

latitude temperatures, atmospheric CO₂, regional vegetation, and AMOC may play roles in modulating long-term EAM variations.

Forcing mechanisms of EASM and EAWM variations

Our newly obtained records show that several short, strengthened EAWM events have occurred during the Holocene (Fig. 4e). These events were probably forced by cold events that occurred in the North Atlantic region (Bond et al., 2001; Menviel et al., 2020; Walczak et al., 2020; Zhang et al., 2021). It is clear that increased DSR events are tightly linked to high-latitude cold events in the North Atlantic region (Bond et al., 2001; Otto-Bliesner et al., 2014), especially during the 12–5 ka period (Fig. 4d and e). Bond events 4 to 8 were found to be well correlated with our DSR records within dating errors, showing that EAWM variations are highly sensitive to high-latitude forcing. However, Bond event 3 was not observed in the ZBT record after 5 ka, and this may have resulted from fewer cold events occurring in the North Atlantic region or from the low-resolution record of the surface loess deposit. The synchrony of the EAM climate and North Atlantic variations has also partly been indicated by previous isotopic records and aeolian sediments along the arid to semiarid transition zone of north-central China (Porter and Zhou, 2006; Wang et al., 2022).

In addition, our findings of a strong EAWM during some part of the Holocene optimum are more surprising, as it was postulated in many previous works that a warm world might reduce the winter monsoon circulation (Ljungqvist et al., 2016), and the warm temperatures and humid climate of the Holocene optimum could be coupled with a weakened EAWM. Because winter insolation, which increased during the Early to Middle Holocene, cannot have affected the strengthened EAWM during the

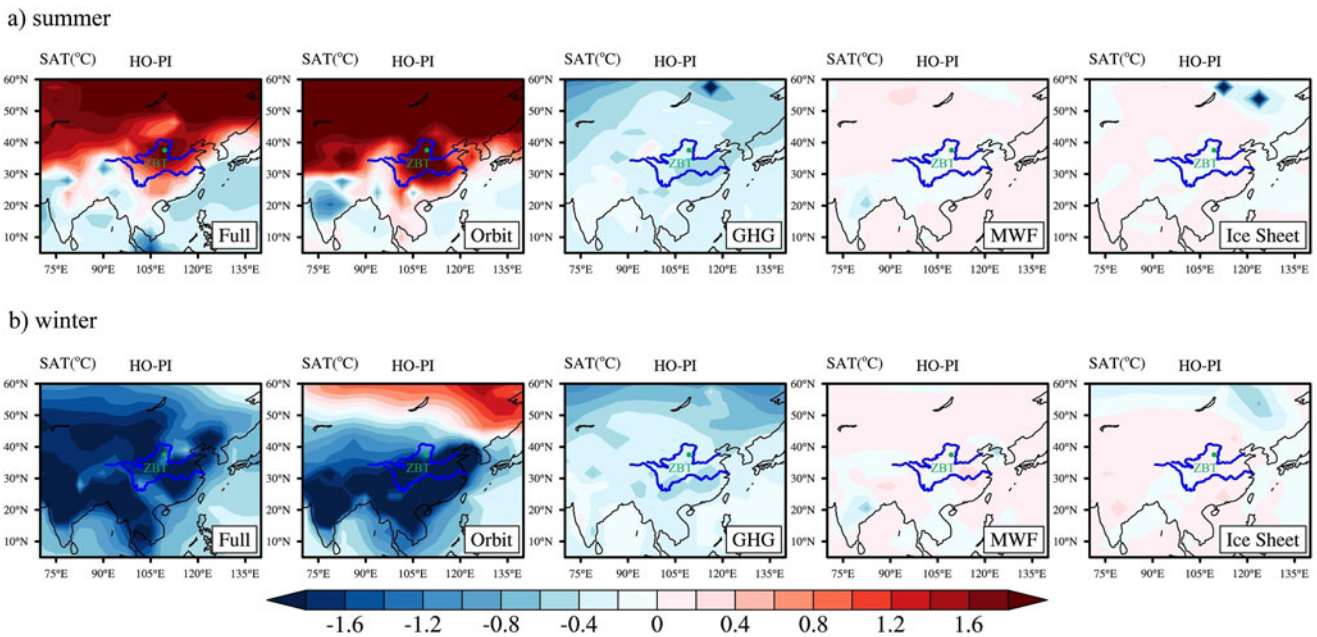


Figure 5. Holocene optimum (7–5 ka) summer (a) and winter (b) surface air temperature (SAT) minus the preindustrial period simulated by TraCE21K, with all forcing (Full), insolation forcing (Orbit), greenhouse gas forcing (GHG), meltwater flux forcing (MWF), and ice-sheet forcing (Ice Sheet). Insolation-forced SAT changes lead to both an increased temperature gradient from land to sea and from high latitudes to low latitudes during summer; thus, both indicate a strengthened East Asian summer monsoon (EASM), while the effects of other forcings are less than those of orbital forcing. During winter, orbital forcing increases the land-to-sea temperature gradient. However, high-latitude temperature exhibits a significant increase, leading to a decreased latitudinal temperature gradient. High-latitude forcing, such as ice-sheet forcing and the effect of the greenhouse gas forcing compensate for high-latitude temperature increase and play an important role in strengthening the East Asian summer winter monsoon (EAWM).

Holocene optimum (Fig. 4a and e), we suggest surface conditions such as relict ice sheets, sea level, and vegetation could have enhanced the seasonality of EASM variations during the Holocene optimum (Fig. 5b, Supplementary Fig. S4b). One interpretation is that cold Bond events at high latitudes have directly facilitated the occurrence of Holocene EAWM events at the Holocene optimum (Fig. 4). Over the optimum period, Bond events 4 and 5, within uncertainty of dating, may have forced increased EAWM events (Fig. 4) through atmospheric bridges such as the westerlies in the Northern Hemisphere (Porter and An, 1995; Zhang et al., 2021). In addition, enhanced EASM circulation has brought more rainfall to this semiarid and arid region, through which surface runoff is strengthened and more sand/silt particle materials are deposited in dust source region, and grass grows during summertime. These processes may have resulted in more surface sediment accumulation on one hand, and vegetation development along with higher temperatures induced evaporation/transpiration on the other hand. Together, these processes caused regional drying and enhanced dust deposition as recorded in high DSR at our site. In addition, from the Early to Middle Holocene, an increase of sea ice in high-latitude led to enhanced albedo, together with a strengthening of Siberian High and a southward migration of the East Asian trough, inducing cooling in midlatitude Asia and strengthening the EAWM (Kaboth-Bahr et al., 2021). Our interpretation is that enhanced seasonality in the EAM determined EASM and EAWM variations during this warm period. Therefore, we suggest that the EASM and EAWM, a regional climatic circulation system in middle latitudes, were modulated by both high-latitude temperature variations and surface feedbacks under a background of insolation variations during the Holocene optimum.

Using boreal summer (June–July–August) precipitation as an index of EASM and boreal winter (December–January–February) wind at 1000 hPa as an EAWM index, the simulated EAM variations over the past 14 ka by the full-forcing TraCE21K model are presented in Figure 4b (Liu et al., 2009). The TraCE21K simulation results show that EASM and EAWM peaked synchronously in the Early Holocene (Fig. 4b, Supplementary Fig. S2, Full), revealing direct insolation forcing. Both EASM precipitation and EAWM wind at 1000 hPa changes during the entire Holocene are dominantly forced by decreasing boreal summer insolation and weakly increasing winter insolation, respectively (Supplementary Fig. S2). However, variations of atmospheric CO₂ forcing, meltwater flux forcing (MWF), and ice-sheet forcing are slight. During the Holocene optimum, EASM responses to low-latitude orbital forcing result from summer temperature increases and enhanced sea-level pressure gradients between the East Asian continent and adjacent oceans (Fig. 5a, Supplementary Fig. S4a). However, variations in winter temperature and sea-level pressure gradient highlight both high- and low-latitude forcings (Fig. 5b, Supplementary Fig. S4b). The mismatch between our proxy record and the modelling results in East Asia reveals that the simulation is based on limited boundary conditions and thus needs further improvement. This is also supported by a recent broadscale pollen assemblage analysis conducted in the Northern Hemisphere, which also revealed widespread model–data contrast (Zhang et al., 2022).

CONCLUSIONS

We find that the EASM and EAWM strengthened simultaneously sometime during the Holocene optimum, with increased

seasonality. In addition, the increased DSR events observed in our records are tightly linked to high-latitude cold events in the Northern Atlantic region, indicating high-latitude modulation of the EAWM. The TraCE21K simulation results show that EASM responses to low-latitude orbital forcing resulted from summer temperature increases and enhanced sea-level pressure gradients, while variations in winter temperature and sea-level pressure gradient highlight both high- and low-latitude forcing. The synchronously strengthened EASM and EAWM during the Holocene optimum demonstrate enhanced seasonality in the EAM during a warm period under the modulation of the high-latitude temperature, low-latitude insolation and regional feedbacks, revealing that the EAM may also exhibit new features under forcing conditions of future global warming by increasing anthropogenic greenhouse gasses.

Supplementary Material. The supplementary material for this article can be found at <https://doi.org/10.1017/qua.2023.76>

Acknowledgments. This research is supported by the National Natural Science Foundation of China (Grant Nos. 42021001, 41920104005, 41971103). All authors declare no conflict of interests relevant to this study.

REFERENCES

- An, Z.S., 2000. The history and variability of the East Asian paleomonsoon climate. *Quaternary Science Reviews* **19**, 171–187.
- Blaauw, M., Christen, J.A., 2011. Flexible paleoclimate age-depth models using an autoregressive gamma process. *Bayesian Analysis*, **6**, 457–474.
- Bond, G., Kromer, B., Beer, J., Muscheler, R., Evans, M.N., Showers, W., Hoffmann, S., Lotti-Bond, R., Hajdas, I., Bonani, G., 2001. Persistent solar influence on north Atlantic climate during the Holocene. *Science* **294**, 2130–2136.
- Bova, S., Rosenthal, Y., Liu, Z., Godad, S.P., Yan, M., 2021. Seasonal origin of the thermal maxima at the Holocene and the last interglacial. *Nature* **589**, 548–553.
- Cai, Y., Cheng, X., Ma, L., Mao, R., Breitenbach, S.F.M., Zhang, H., Xue, G., Cheng, H., Edwards, R.L., An, Z.S., 2021. Holocene variability of East Asian summer monsoon as viewed from the speleothem $\delta^{18}\text{O}$ records in central China. *Earth and Planetary Science Letters* **558**, 116758.
- Chen, F., Xu, Q., Chen, J., Birks, H.J., Liu, J., Zhang, S., Jin, L., et al., 2015. East Asian summer monsoon precipitation variability since the last deglaciation. *Scientific Reports* **5**, 11186.
- Ding, Z.L., Derbyshire, E., Yang, S. L., Sun, J.M., Liu, T.S., 2005. Stepwise expansion of desert environment across northern China in the past 3.5 Ma and implications for monsoon evolution. *Earth and Planetary Science Letters* **237**, 45–55.
- Gong, X.J., Wang, P., Yang, Z.J., Dong, Q. Y., Song, C., Guo, J., Chen, H.Y., 2021. Climate change recorded by the grain size end member since MIS 3 in Jingbian area. *Bulletin of Geological Science and Technology* **40**, 184–191.
- Hajdas, I., 2008. Radiocarbon dating and its applications in Quaternary studies. *E&G Quaternary Science Journal* **57**, 2–24.
- He, C., Liu, Z., Otto-Bliesner, B.L., Brady, E.C., Zhu, C., Tomas, R., Clark, P., et al., 2021. Hydroclimate footprint of pan-Asian monsoon water isotope during the last deglaciation. *Science Advances* **7**. <http://dx.doi.org/10.1126/sciadv.abe2611>.
- He, F., Clark, P.U., 2022. Freshwater forcing of the Atlantic Meridional Overturning Circulation revisited. *Nature Climate Change* **12**, 449–454.
- Hua, Q., Barbetti, M., Rakowski, A.Z., 2013. Atmospheric radiocarbon for the period 1950–2010. *Radiocarbon* **55**, 2059–2072.
- Jia, G.D., Bai, Y., Yang, X.Q., Xie, L.H., Wei, G.J., Ouyang, T.P., Chu, G.Q., Liu, Z.H., Peng, P.A., 2015. Biogeochemical evidence of Holocene East Asian summer and winter monsoon variability from a tropical maar lake in southern China. *Quaternary Science Reviews* **111**, 51–61.
- Jiang, W., Cheng, Y., Yang, X., Yang, S., Wan, S., 2013. Chinese Loess Plateau vegetation since the Last Glacial Maximum and its implications for vegetation restoration. *Journal of Applied Ecology* **50**, 440–448.

- Kaboth-Bahr, S., Bahr, A., Zeeden, C., Yamoah, K.A., Lone, M.A., Chuang, C.-K., Lowemark, L., Wei, K.Y., 2021. A tale of shifting relations: East Asian summer and winter monsoon variability during the Holocene. *Scientific Reports* **11**, 1–10.
- Kanamitsu, M., Ebisuzaki, W., Woollen, J., Yang, S.K., Hnilo, J.J., Fiorino, M., Potter, G.L., 2002. NCEP-DOE AMIP-II reanalysis (R-2). *Bulletin of the American Meteorological Society* **83**, 1631–1643.
- Kang, S., Du, J., Wang, N., Dong, J., Song, Y., 2020. Early Holocene weakening and mid- to late Holocene strengthening of the East Asian winter monsoon. *Geology* **48**, 1043–1047.
- Laskar, J., Robutel, P., Joutel, F., Gastineau, M., Correia, A.C.M., Levrard, B., 2004. A long-term numerical solution for the insolation quantities of the Earth. *Astronomy & Astrophysics* **428**, 261–285.
- Li, J.J., Feng, Z.D., Tang, L.Y., 1988. Late Quaternary monsoon patterns on the loess plateau of China. *Earth Surface Processes and Landforms* **13**, 125–135.
- Liang, C.H., Lu, H., Gu, Y., Zhao, C., Liu, W., Zhang, X., Zhang, H., 2022. Asynchronous variations of East Asian summer monsoon, vegetation and soil formation at Yulin (north China) in the Holocene. *Journal of Quaternary Science* **37**, 1083–1090.
- Liu, Z., Otto-Bliesner, B.L., He, F., Brady, E.C., Tomas, R., Clark, P.U., Carlson, A.E., et al., 2009. Transient simulation of last deglaciation with a new mechanism for Bolling-Allerod warming. *Science* **325**, 310–314.
- Ljungqvist, F.C., Krusic, P.J., Sundqvist, H.S., Zorita, E., Brattstrom, G., Frank, D., 2016. Northern Hemisphere hydroclimate variability over the past twelve centuries. *Nature* **532**, 94–98.
- Lu, H.Y., Sun, D.H., 2000. Pathways of dust input to the Chinese Loess Plateau during the last glacial and interglacial periods. *Catena* **40**, 251–261.
- Lu, H.Y., Miao, X.D., Zhou, Y.L., Mason, J., Swinehart, J., Zhang, J.F., Zhou, L.P., Yi, S.W., 2005. Late Quaternary aeolian activity in the Mu Us and Otindag dune fields (north China) and lagged response to insolation forcing. *Geophysical Research Letters* **32**. <http://dx.doi.org/10.1029/2005GL024560>.
- Lu, H.Y., Mason, J.A., Stevens, T., Zhou, Y.L., Yi, S.W., Miao, X.D., 2011. Response of surface processes to climatic change in the dunefields and Loess Plateau of north China during the late Quaternary. *Earth Surface Processes and Landforms* **36**, 1590–1603.
- Lu, H.Y., Yi, S.W., Liu, Z.Y., Mason, J.A., Jiang, D.B., Cheng, J., Stevens, T., et al., 2013a. Variation of East Asian monsoon precipitation during the past 21 k.y. and potential CO₂ forcing. *Geology* **41**, 1023–1026.
- Lu, H.Y., Yi, S.W., Xu Z.W., Zhou, Y.L., Zeng, L., Zhu, F. Y., Feng, H., et al., 2013b. Chinese deserts and sand fields in Last Glacial Maximum and Holocene Optimum. *Chinese Science Bulletin* **58**, 2775–2783.
- Lu, H.Y., Wang, X., Wang, Y., Zhang, X., Markovi, S.B., 2022. Chinese loess and the Asian monsoon: what we know and what remains unknown. *Quaternary International* **620**, 85–97.
- Mason, J.A., Nater, E.A., Zanner, C.W., Bell, J.C., 1999. A new model of topographic effects on the distribution of loess. *Geomorphology* **28**, 223–236.
- Menviel, L.C., Skinner, L.C., Tarasov, L., Tzedakis, P. C., 2020. An ice-climate oscillatory framework for Dansgaard-Oeschger cycles. *Nature Reviews Earth & Environment* **1**, 677–693.
- Otto-Bliesner, B.L., Russell, J.M., Clark, P.U., Liu, Z.Y., Overpeck, J.T., Konecky, B., deMenocal, P., Nicholson, S.E., He, F., Lu, Z.Y., 2014. Coherent changes of southeastern equatorial and northern African rainfall during the last deglaciation. *Science* **346**, 1223–1227.
- Porter, S.C., An, Z.S., 1995. Correlation between climate events in the North-Atlantic and China during Last Glaciation. *Nature* **375**, 305–308.
- Porter, S.C., Zhou, W.J., 2006. Synchronism of Holocene East Asian monsoon variations and North Atlantic drift-ice tracers. *Quaternary Research* **65**, 443–449.
- Pye, K., 1995. The nature, origin and accumulation of loess. *Quaternary Science Reviews* **14**, 653–667.
- Ramsey, C.B., 2009. Bayesian analysis of radiocarbon dates. *Radiocarbon* **51**, 337–360.
- Reimer, P.J., Austin, W.E.N., Bard, E., Bayliss, A., Blackwell, P.G., Ramsey, C.B., Butzin, M., et al., 2020. The Intcal20 Northern Hemisphere radiocarbon age calibration curve (0–55 cal kBP). *Radiocarbon* **62**, 725–757.
- Routson, C.C., Mckay, N.P., Kaufman, D.S., Erb, M.P., Goosse, H., Shuman, B.N., Rodysill, J.R., Ault, T., 2019. Mid-latitude net precipitation decreased with Arctic warming during the Holocene. *Nature* **568**, 83–87.
- Steinke, S., Glatz, C., Mohtadi, M., Groeneveld, J., Li, Q.Y., Jian, Z.M., 2011. Past dynamics of the East Asian monsoon: no inverse behaviour between the summer and winter monsoon during the Holocene. *Global Planet Change* **78**, 170–177.
- Sun, W.Y., Liu, J., Wan, L.F., Ning, L., Yan, M., 2020. Simulation of northern hemisphere mid-latitude precipitation response to different external forcings during the Holocene. *Quaternary Sciences* **40**, 1588–1596.
- Synal, H. A., Stocker, M., Suter, M., 2007. MICADAS: a new compact radiocarbon AMS system. *Nuclear Instruments and Methods in Physics Research Section B: Beam Interactions with Materials and Atoms* **259**, 7–13.
- Ujvari, G., Kok, J.F., Varga, G., Kovacs, J., 2016. The physics of wind-blown loess: implications for grain size proxy interpretations in Quaternary paleoclimate studies. *Earth-Science Reviews* **154**, 247–278.
- Ujvari, G., Stevens, T., Molnar, M., Demeny, A., Lambert, F., Varga, G., Jull, A.J.T., Pall-Gergely, B., Buylaert, J.P., Kovacs, J., 2017. Coupled European and Greenland last glacial dust activity driven by North Atlantic climate. *Proceedings of the National Academy of Sciences USA* **114**, E10632–E10638.
- Walczak, M.H., Mix, A.C., Cowan, E.A., Fallon, S., Fifield, L.K., Alder, J.R., Du, J.H., et al., 2020. Phasing of millennial-scale climate variability in the Pacific and Atlantic Oceans. *Science* **370**, 716–720.
- Wang, B., Biasutti, M., Byrne, M.P., Castro, C., Chang, C.-P., Cook, K., Fu, R., et al., 2021. Monsoons climate change assessment. *Bulletin of the American Meteorological Society* **102**, E1–E19.
- Wang, F., Si, Y., Li, B., Niu, D., Li, Z., Wen, X., Yang, Z., 2022. Variations in the aeolian sequence Zr/Rb ratios in the Mu Us Desert during the Holocene and their implications for the East Asian monsoon. *Aeolian Research* **54**, 100753.
- Wang, H.L., Lu, H.Y., Zhang, H.Y., Yi, S.W., Gu, Y., Liang, C.H., 2019. Grass habitat analysis and phytolith-based quantitative reconstruction of Asian monsoon climate change in the sand-loess transitional zone, northern China. *Quaternary Research* **92**, 519–529.
- Wang, J.J., Lu, H.Y., Cheng, J., Zhao, C., 2023. Global terrestrial monsoon area variations since Last Glacial Maximum based on TraCE21ka and PMIP4-CMIP6 simulations. *Global and Planetary Change* **231**, 104308.
- Wang, L., Li, J.J., Lu, H.Y., Gu, Z.Y., Rioual, P., Hao, Q.Z., Mackay, A.W., et al., 2012. The East Asian winter monsoon over the last 15,000 years: its links to high-latitudes and tropical climate systems and complex correlation to the summer monsoon. *Quaternary Science Reviews* **32**, 131–142.
- Wang, Y.J., Cheng, H., Edwards, R.L., He, Y.Q., Kong, X.G., An, Z.S., Wu, J.Y., Kelly, M.J., Dykoski, C.A., Li, X.D., 2005. The Holocene Asian monsoon: links to solar changes and North Atlantic climate. *Science* **308**, 854–857.
- Wen, X.H., Li, B.S., Zheng, Y.M., Yang, Q.J., Niu, D.F., Shu, P.X., 2016. Early Holocene multi-centennial moisture change reconstructed from lithology, grain-size and chemical composition data in the eastern Mu Us desert and potential driving forces. *Palaeogeography, Palaeoclimatology, Palaeoecology* **459**, 440–452.
- Wen, X.Y., Liu, Z.Y., Wang, S.W., Cheng, J., Zhu, J., 2016. Correlation and anti-correlation of the East Asian summer and winter monsoons during the last 21,000 years. *Nature Communications* **7**. <http://dx.doi.org/10.1038/ncomms11999>.
- Wu, J., Lu, H.Y., Yi, S.W., Xu, Z.W., Gu, Y., Liang, C.H., Cui, M.C., Sun, X.F., 2019. Establishing a high-resolution luminescence chronology for the Zhenbeitai sand-loess section at Yulin, north-central China. *Quaternary Geochronology* **49**, 78–84.
- Xu, Z. W., Mason, J.A., Xu, C., Yi, S.W., Bathiany, S., Yizhaq, H., Zhou, Y.L., Cheng, J., Holmgren, M., Lu, H.Y., 2020. Critical transitions in Chinese dunes during the past 12,000 years. *Science Advances* **6**. <http://dx.doi.org/10.1126/sciadv.aay8020>.
- Yang, S.L., Ding, Z.L., 2008. Advance-retreat history of the East-Asian summer monsoon rainfall belt over northern China during the last two glacial-interglacial cycles. *Earth and Planetary Science Letters* **274**, 499–510.
- Yang, S.L., Ding, Z.L., Li, Y.Y., Wang, X., Jiang, W.Y., Huang, X.F., 2015. Warming-induced northwestward migration of the East Asian

monsoon rain belt from the Last Glacial Maximum to the mid-Holocene. *Proceedings of the National Academy of Sciences USA* **112**(43), 13178–13183.

Zhang, W.C., Wu, H.B., Cheng, J., Geng, J.Y., Li, Q., Sun, Y., Yu, Y.Y., Lu, H.Y., Guo, Z.T., 2022. Holocene seasonal temperature evolution and spatial

variability over the Northern Hemisphere landmass. *Nature Communications* **13**. <http://dx.doi.org/10.1038/s41467-022-33107-0>.

Zhang, X., Barker, S., Knorr, G., Lohmann, G., Drysdale, R., Sun, Y., Hodell, D., Chen, F.H., 2021. Direct astronomical influence on abrupt climate variability. *Nature Geoscience* **14**, 819–826.